Chem

Article

CO$_2$ Hydrogenation to Ethanol over Cu@Na-Beta

$$2CO_2 + 6H_2 \longrightarrow C_2H_5OH + 3H_2O$$

Liping Ding, Taotao Shi, Jing Gu, ..., Yan Zhu, Zhaoxu Chen, Weiping Ding

zxchen@nju.edu.cn (Z.C.)
dingwp@nju.edu.cn (W.D.)

HIGHLIGHTS

Ethanol as the only organic product obtained from high-performance CO$_2$ hydrogenation

Key step for C–C bond is achieved between CO$_2$ and surface methyl at Cu step sites

Current ethanol synthesis from CO$_2$ hydrogenation should be useful in industry

Assemblies of surroundings and reactive centers are important for novel catalysts

CO$_2$ direct reduction to ethanol is a much-anticipated research topic worldwide. A big progress has been made in the current investigation toward industry application. A high-performance catalyst Cu@Na-Beta, prepared via a unique method to embed 2~5 nm Cu nanoparticles in crystalline particles of Na-Beta zeolite, is reported for CO$_2$ hydrogenation to ethanol in a traditional fixed-bed reactor, with ethanol space-time yield of ~398 mg·g$_{cat}^{-1}$·h^{-1}. Peripherals-surrounded catalysts, which may be called mesocatalysts, appear to be one focus of future investigations on catalysis.

Q8

Chem

CellPress

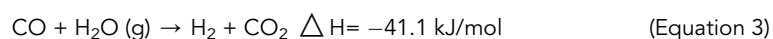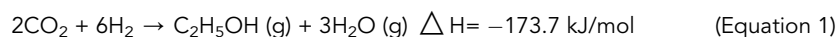Article

CO$_2$ Hydrogenation to Ethanol over Cu@Na-Beta

Liping Ding,[1,4] Taotao Shi,[1,4] Jing Gu,[1] Yun Cui,[1] Zhiyang Zhang,[1] Changju Yang,[1] Teng Chen,[1] Ming Lin,[2] Peng Wang,[3] Nianhua Xue,[1] Luming Peng,[1] Xuefeng Guo,[1] Yan Zhu,[1] Zhaoxu Chen,[1,*] and Weiping Ding[1,5,*]

SUMMARY

Here, we report a high-performance catalyst Cu@Na-Beta, prepared via a unique method to embed 2∼5 nm Cu nanoparticles in crystalline particles of Na-Beta zeolite, for CO$_2$ hydrogenation to ethanol as the only organic product in a traditional fixed-bed reactor. The ethanol yield in a single pass can reach ∼14% at 300°C, ∼12,000 mL·g$_{cat}^{-1}$·h^{-1}, and 2.1 MPa, corresponding to a space-time yield of ∼398 mg·g$_{cat}^{-1}$·h^{-1}. The key step of the reaction is considered as the rapid bonding of CO$_2$* with surface methyl species at step sites of Cu nanoparticles to CH$_3$COO* that converts to ethanol in following hydrogenation steps. The points of the catalyst seemed to be that the irregular copper nanoparticles stuck in zeolitic frameworks offer high density of step sites and the intimate surrounding of zeolitic frameworks strongly constrain the CO$_2$ reactions at the copper surface and block by-products, such as methanol, formic acid, and acetyl acid.

INTRODUCTION

The utilization of carbon dioxide has a massive impact on carbon cycling for the development of the recycling economy[1,2] and has attracted much research attention worldwide. Among the products from CO$_2$ conversion, methanol as the main product has been investigated intensively in recent years.[3–5] Comparatively, few results have been reported about the synthesis of ethanol or C$_{2+}$OH from CO$_2$ hydrogenation, even though ethanol is not only a nontoxic but also a more valuable product that can be easily converted to high-value chemicals such as ethylene. Considering the synthetic routes of ethanol from feed gases of CO$_2$+3H$_2$ or CO+2H$_2$, the relevant reactions are shown as Equations 1, 2, and 3. This means that the hydrogenation of CO$_2$ to ethanol highly relates to the syngas conversion and the difference is just the water-gas shift reaction, a well-established industrial reaction.[6] As to the utilization of chemical energy included in the feed gases, one C$_2$H$_5$OH (g) reserves ∼94% or ∼89% chemical energy included in 6H$_2$ or 2CO+4H$_2$, respectively, reflecting to some extent the advantages of CO$_2$ hydrogenation to ethanol over the syngas conversion.

$$2CO_2 + 6H_2 \rightarrow C_2H_5OH\ (g) + 3H_2O\ (g)\ \triangle H= -173.7\ kJ/mol \qquad \text{(Equation 1)}$$

$$2CO + 4H_2 \rightarrow C_2H_5OH\ (g) + H_2O\ (g)\ \triangle H= -255.9\ kJ/mol \qquad \text{(Equation 2)}$$

$$CO + H_2O\ (g) \rightarrow H_2 + CO_2\ \triangle H= -41.1\ kJ/mol \qquad \text{(Equation 3)}$$

The Bigger Picture

The high-performance catalyst Cu@Na-Beta, prepared via a unique method to embed 2∼5 nm Cu nanoparticles in crystalline particles of Na-Beta zeolite, is reported for CO$_2$ hydrogenation to ethanol as the only organic product in a traditional fixed-bed reactor. The ethanol yield in a single pass can reach ∼14% at 300°C, ∼12,000 mL·g$_{cat}^{-1}$·h^{-1}, and 2.1 MPa, corresponding to space-time yield of ∼398 mg·g$_{cat}^{-1}$·h^{-1}. The key step of the reaction is the rapid bonding of CO$_2$* with surface methyl species at step sites of Cu nanoparticles to CH$_3$COO*, which converts to ethanol in the following hydrogenation steps. The points of the catalyst seem to be that the irregular copper nanoparticles stuck in zeolitic frameworks offer a high density of step sites and that the intimate surrounding of zeolitic frameworks strongly constrains the CO$_2$ reactions at the copper surface and blocks byproducts such as methanol, formic acid, and acetyl acid.

For the practical use of CO$_2$ hydrogenation to ethanol, a significant promotion on catalytic efficiency and ethanol selectivity is highly desired.[7–15] At the present time, it is a great challenge to obtain high or ideally exclusive selectivity to ethanol by using traditional heterogeneous catalysts at valuably high CO$_2$ conversion. New ideas for the catalyst design are called to achieve high ethanol selectivity as well as a high activity for CO$_2$ conversion.

Copper-based catalysts have been widely applied to catalyze the hydrogenation of CO$_x$ and the production of organic oxygenates from syngas,[16–18] of which the activity and selectivity strongly depend on the support and/or promoters. Especially, Liao et al. have revealed the importance of morphology-dependent interactions of ZnO with Cu nanoparticles at the interface in between in selective hydrogenation of CO$_2$ to CH$_3$OH.[16] On the other hand, zeolites with well-organized 3D porous structure have strong confining or modulating effects on entering molecules and the clusters enclosed, as reported in the recent years.[19–22] Zeolite beta is a disordered intergrown hybrid of tetragonal and clinorhombic system, which are two distinct but closely related structures and possesses a three-dimensional pore system containing 12-membered ring apertures. The inner field potential of Beta zeolite has fascinating characteristics, different from the surrounding effects of the ZSM-5 and X zeolites, which we have reported earlier.[19,22] In current work, we combined the Beta zeolite and the active Cu nanoparticles to prepare a highly efficient catalyst, in an intimately cooperated structure with copper enclosed in crystalline particles of zeolite Beta, which showed the superior performance for CO$_2$ hydrogenation to ethanol. The CuO nanoparticles were embedded in crystal particles of Na-Beta zeolite (abbreviated as CuO@Na-Beta) by a two-step preparation procedure using dry gel conversion and crystallization methods (Preparation of Catalysts), similar to what we previously described.[19] Then the sample was reduced by hydrogen to Cu@Na-Beta before the catalytic reaction. The obtained material is considered as ∼2–5 nm Cu nanoparticles embedded in the zeolite crystal particles, as characterized by various techniques (see Experimental Procedures).

RESULTS AND DISCUSSION

The equilibrium conversions of CO$_2$ with the mixture of CO$_2$+3H$_2$ as reactants at different temperatures and pressures were calculated according to thermodynamic parameters of the related compounds (Supplemental Information; Figure S1), implying the reaction conditions for ethanol synthesis from CO$_2$ hydrogenation can be quite mild. Figures 1A–1D show the catalytic performance of the catalyst, ∼8.24 wt % Cu@Na-Beta (the Cu content was measured by X-ray fluorescence [XRF] spectroscopy) for CO$_2$ hydrogenation. With the reaction temperature increasing from 200°C to 350°C, the conversion of CO$_2$ increases from 0.85% to 12.2% at a rather high space velocity 12,000 mL·g$_{cat}^{-1}$·h^{-1} and a pressure of mere 1.3 MPa. When the temperature reaches 250°C, CO appears as a by-product and the selectivity of CO increases to ∼45.2% as the temperature increases to 350°C (Figure 1A), while the ethanol is the only organic product. The pressure has a great effect on the performance of the catalyst. When the pressure changes from 0.5 to 2.1 MPa (300°C), the conversion of CO$_2$ increases significantly from ∼2.0% to ∼18% and the selectivity of CO decreases from 94.6% to 21% (Figure 1B), and ethanol is still the only organic product observed in the tests of the reaction. When the space velocity increases from 6,000 to 18,000 mL·g$_{cat}^{-1}$·h^{-1}, the CO$_2$ conversion decreases from 13.5% to 3.7%, and the CO selectivity increases from ∼26.9% to ∼35.9% (Figure 1C). The ethanol yield of ∼14 % is obtained at 300°C, 2.1 Mpa, and 12,000 mL·g$_{cat}^{-1}$·h^{-1}.

[1]Key Laboratory of Mesoscopic Chemistry, School of Chemistry and Chemical Engineering, Nanjing University, Nanjing 210093, China

[2]Institute of Materials Research and Engineering, Agency for Science, Technology and Research (A*STAR), 3 Research Link, Singapore 117602, Singapore

[3]National Laboratory of Solid State Microstructures, College of Engineering and Applied Sciences and Collaborative Innovation Center of Advanced Microstructures, Nanjing University, Nanjing 210093, China

[4]These authors contributed equally

[5]Lead Contact

*Correspondence: zxchen@nju.edu.cn (Z.C.), dingwp@nju.edu.cn (W.D.)

https://doi.org/10.1016/j.chempr.2020.07.001

Chem
Article

CellPress
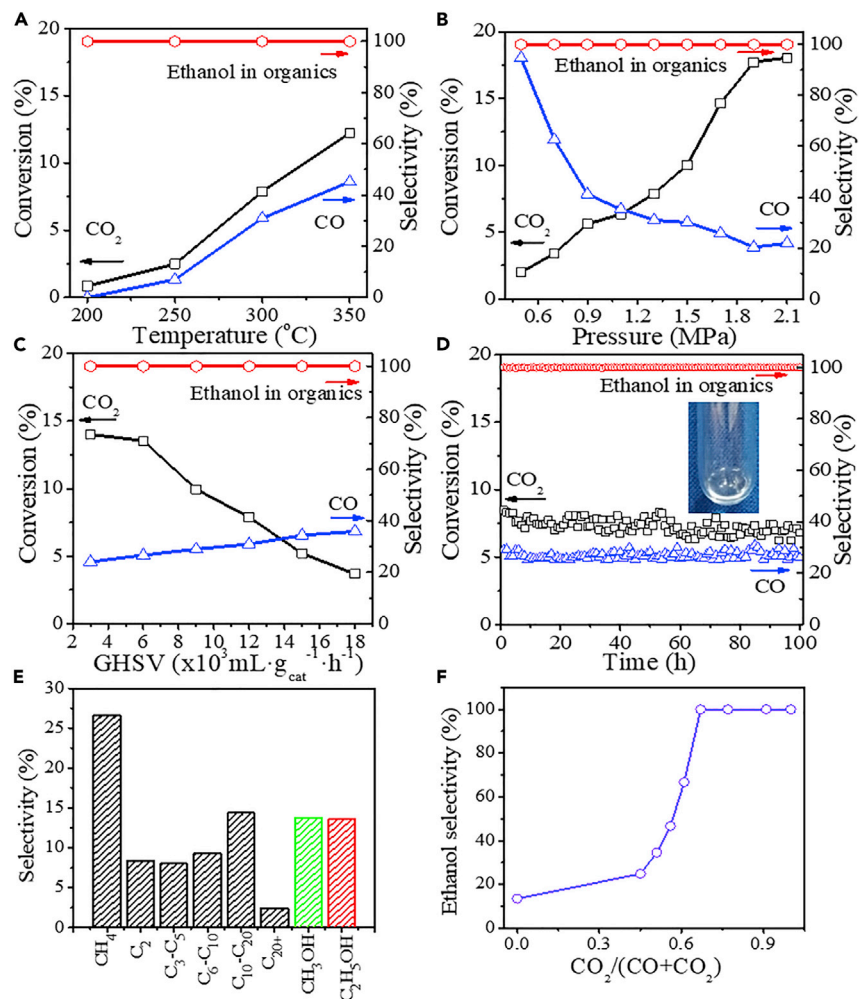
Figure 1. Catalytic Performance of the Cu@Na-Beta Catalyst

(A) Effect of reaction temperature (12,000 mL·g_{cat}^{-1}·h^{-1}; 1.3 MPa; CO$_2$+3H$_2$).

(B) Effect of reaction pressure (12,000 mL·g_{cat}^{-1}·h^{-1}; 300°C; CO$_2$+3H$_2$).

(C) Effect of space velocity (1.3MPa; 300°C; CO$_2$+3H$_2$).

(D) Prolonged test of reaction (300°C; 1.3 MPa; 12,000 mL·g_{cat}^{-1}·h^{-1}; CO$_2$+3H$_2$. Inset: Products collected by a condenser during the first 24 h of reaction).

(E) The product selectivities for syngas conversion (1.5 MPa; 12,000 mL·g_{cat}^{-1}·h^{-1}; 300°C; CO+2H$_2$).

(F) Ethanol selectivity in organic products using the mixture of CO, CO$_2$, and H$_2$ as reactants (1.5 MPa; 12,000 mL·g_{cat}^{-1}·h^{-1}; 300°C).

More importantly, the catalytic performance of the catalyst Cu@Na-Beta remains stable during the 100-h reaction on stream (Figure 1D), and ethanol is the only organic product formed under the reaction conditions (H$_2$/CO$_2$ = 3/1, 300°C, 1.3 MPa, 12,000 mL·g_{cat}^{-1}·h^{-1}). The products of the first 24-h reaction during the prolonged test have been collected with a condenser cooled by liquid nitrogen. The weight of the products obtained is ∼0.71 g, in the composition of ∼43.5 wt % ethanol, coincidently according to the stoichiometry of the reaction 2CO$_2$ + 6H$_2$ = C$_2$H$_5$OH + 3H$_2$O, as analyzed by gas chromatography (GC) using acetone as inner standard. Referring to the collection result, the isolated yield of ethanol is calculated as ∼5.1%, which is in accordance with the analysis results by online GC. The NMR

Table 1. Catalytic Performance of Some Related Catalysts for CO_2 Hydrogenation

Catalyst	P (MPa)	T (°C)	Conv. (%)	Sel. (%)[b]				STY[c]	Ref
				CH_4	CH_3OH	C_2H_5OH	CO		
Cu/SiO2[a]	1.3	300	0.47	N/D	~100	N/D	41.6	0 (0)	This work
Cu/Na-Beta[a]			3.1	5.6	30.1	64.3	66.4	46 (3.0)	
Cu@Na-ZSM5[a]			1.8	6.8	8.2	85.0	25.4	59 (3.9)	
Cu@Na-Beta[a]			7.9	N/D	N/D	~100	30.5	258 (17.1)	
Ru-Fe/SiO2	5.0	260	26.7	34.7	29.4	16	19.7	–	Kusama et al.[7]
CoMoS	10.3	340	32	36.7	47.1	12.9	57.5	–	Nieskens et al.[8]
CuZnFe0.5K0.15	6.0	300	42.3	56.4	4.7	32 (C2+)	6.9	148(C2+)	Li et al.[9]
K-CuCo/MoOx[d]	4.0	270	–	–	–	–	–	27 (C2+)	Prieto et al.[10]
Pt/Co3O4	8.0	200	–	–	12.5	57	–	0.29	He et al.[11]
Co/Mo2C	4.0	200	~10	9.5	46	25	9.5	–	Chen et al.[12]
Pd2Cu/P25	3.2	200	–	–	–	92	–	41.5	Bai et al.[13]
CoAlOx	4.0	140	–		–	92.1	–	0.444	Wang et al.[14]
Meso Carbon[e]	−0.56 V		–		–	100	–	–	Song et al.[15]

[a]CO is not included to calculate the organic product selectivity.
[b]Space-time yield of ethanol ($mg \cdot g_{cat}^{-1} \cdot h^{-1}$). Data in parentheses are turnover frequencies (TOF in h^{-1}).
[c]0.1 g Cat; GHSV: 12,000 $mL \cdot g_{cat}^{-1} \cdot h^{-1}$.
[d]CO hydrogenation to ethanol.
[e]Electroreduction of CO_2 to ethanol.

spectrum of the liquid product collected is also listed in Figure S2 and only the signals from ethanol and water are observed.

It is very interesting that the catalyst gives totally different results with syngas $CO+2H_2$ used as the reactants, of which products similar to Fischer-Tropsch synthesis are obtained, even though some methanol and ethanol are also produced, as shown in Figure 1E. If the mixture of CO, CO_2, and H_2 was used as the feed gas, the ethanol became the only organic product with a ratio of $CO_2/(CO + CO_2)$ in the feed gas larger than 0.65, indicating the CO_2 is important for the formation of ethanol (Figure 1F).

For insight into the catalytic mechanism, three control samples were prepared with the same copper content. Two of them were prepared by traditionally impregnated copper over Na-Beta zeolite (Cu/Na-Beta) and silica (Cu/SiO2). The third control sample was Cu@Na-ZSM-5, which was prepared using the same method as Cu@Na-Beta with Na-ZSM-5 zeolite. The typical catalytic performances of the catalysts for the title reaction are listed in Table 1. Under the same reaction conditions, the catalyst Cu/SiO2 shows poor activity for CO_2 conversion, and no ethanol is detected in products and the results seem consistent with that reported by Wang et al.,[23] in which the Cu/SiO2 needed higher pressure to promote its activity. Comparatively, the Cu/Na-Beta is active for CO_2 conversion and ethanol formation but much inferior to the Cu@Na-Beta, and the yield of ethanol over the former is only ~16% of the latter. The catalyst Cu@Na-ZSM-5 shows fairly good catalytic performance but the selectivity to ethanol is not exclusive and methanol and methane are detected. The results of the papers published on conversion of CO_2 to ethanol are listed in Table 1. Among traditional catalysts, the results reported by this work are much more excellent for the selectivity of ethanol. Almost 100% selectivity to ethanol can be achieved by electroreduction over nitrogen-doped mesocarbon; however, the conversion of CO_2 is low. These experimental results suggest that

CellPress
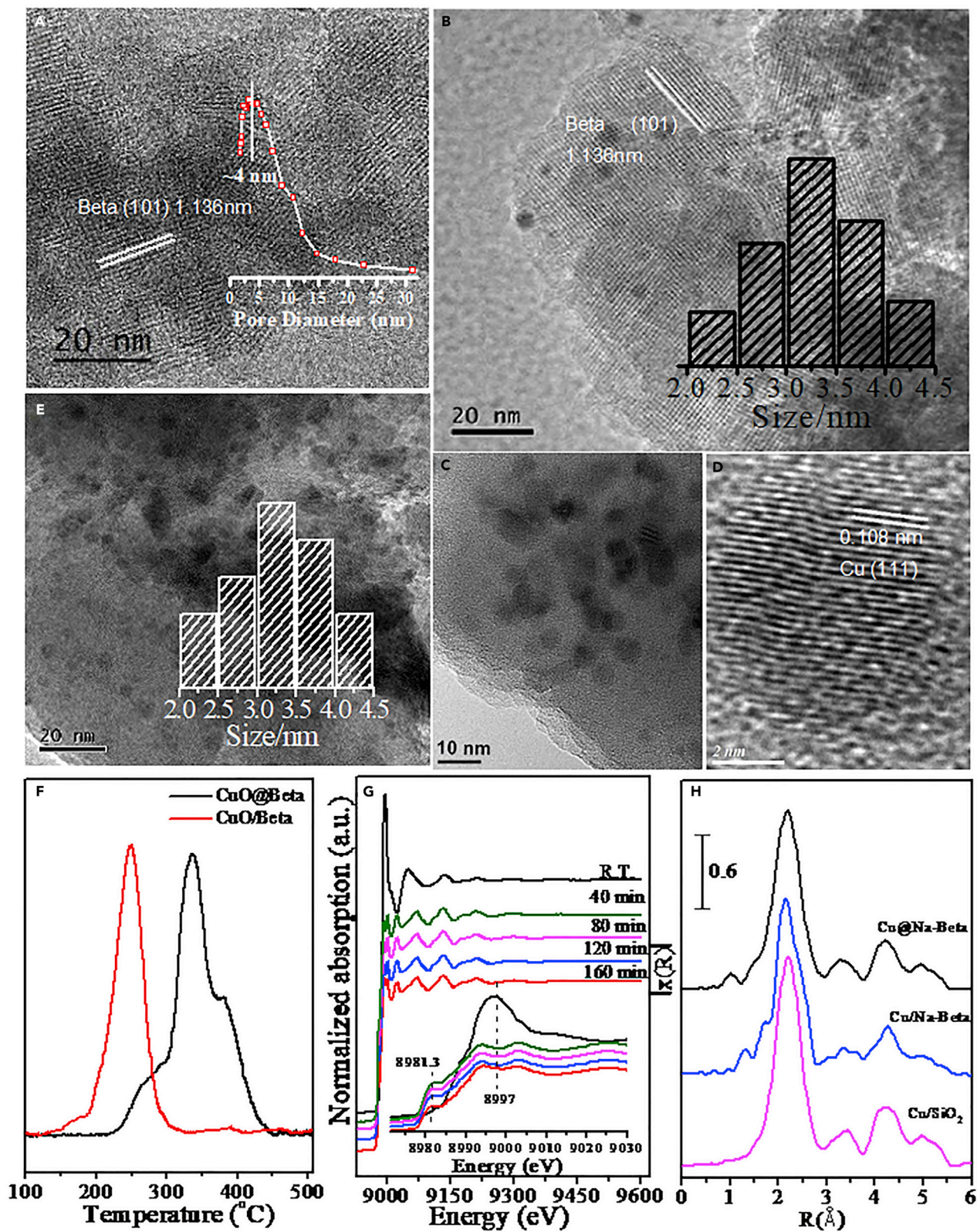
Figure 2. The Characterization of the Catalyst Cu@Na-Beta at Different Status

(A) TEM image of the Na-Beta zeolite and the pore-size distribution obtained from N$_2$ sorption (inset) of the zeolite treated by alkaline solution for formation of irregular mesopores.

(B) HRTEM image of Cu@Na-Beta reduced from CuO@Na-Beta and the size distribution of Cu nanoparticles (inset).

(C) HRTEM of copper nanoparticles in Cu@Na-Beta.

(D) HRTEM of a Cu nanoparticle in Cu@Na-Beta (the same sample with C).

(E) TEM image of spent Cu@Na-Beta after a long-term reaction (100 h) and the size distribution of Cu nanoparticles (inset).

(F) H$_2$-TPR of samples of CuO@Na-Beta and CuO/Na-Beta.

(G) Operando X-ray absorption spectra (XAS) of CuO@Na-Beta recorded every 40 min from its contact with reaction gases (0.5 MPa, H$_2$/CO$_2$ = 3:1, 250°C).

(H) Radial distribution functions of Cu from Fourier transformed k-edge of Cu EXAFS of the samples Cu@Na-Beta, Cu/Na-Beta, and Cu/SiO$_2$.

the zeolites and the cooperation manner between the zeolites and copper are important to obtain the excellent catalytic performance and the enclosure of copper nanoparticles in the crystal particles of Beta zeolite is the key factor. The intimate cooperation or synergism between them, however, appears different from previously reported remarkable results on syngas conversion using Ox-Zel catalysts, in which the bifunctional catalytic mechanism is established, i.e., CO hydrogenation on oxides to intermediates that are further converted to hydrocarbons on acidic SAPO-34 or H-ZSM-5 at distance, as reported by Bao et al. and Wang et al.[24,25] For current Cu@Na-Beta catalyst, the surrounding Na-Beta framework constrains the copper nanoparticles at special shapes and electronic status suitable for the CO$_2$ hydrogenation to ethanol occurr at the nanoparticles, and the enveloping of zeolitic frameworks on the nanoparticle surface is also highly influential, which restricts side reactions for the production of methanol, formic acid, acetic acid, etc.

Figure 2 shows the characterization results of the related samples. The alkali-treatment on raw Na-Beta zeolite led to the formation of mesopores in their crystal particles, and the sizes of the mesopores were measured by N$_2$ sorption as ∼4 nm (Figure 2A and inset). CuO nanoparticles were introduced into the mesopores and then enclosed in the interior of the zeolite crystal particles after the two-step dry gel conversion (DGC) synthesis. After a reduction in 5% H$_2$/N$_2$ at 350°C, the CuO@Na-Beta was reduced to Cu@Na-Beta and the copper species remain as highly dispersed nanoparticles enclosed in the Beta zeolite crystal particles, as shown in Figure 2B. HRTEM of irregular copper nanoparticles in Cu@Na-Beta is shown in Figure 2C. The irregular shape of Cu nanoparticles was embedded in Na-Beta zeolites. The high-resolution image of a copper particle in a gourd shape enclosed in the zeolite is shown in Figures 2D and S3A. By the difficultly obtained image, the copper nanoparticle enclosed in the zeolite is constructed as accurately as possible and shown in Figure S3B. It appears that step sites show up on the particle surface, due to the constraint of the irregular mesopores of the zeolite etched by alkali during the preparation. After a long-term reaction of 100 h, the copper nanoparticles retain their original sizes, as revealed by the TEM image of spent Cu@Na-Beta (Figure 2E), in agreement with its stable catalytic performance, as shown in Figure 1D. The XRD (X-ray diffraction) patterns of related samples are shown in Figure S4, indicating the reduction of CuO to metallic copper during the treatment in 5% H$_2$/N$_2$ at 350°C. The crystallinities of the zeolite in CuO@Na-Beta, Cu@Na-Beta, and spent Cu@Na-Beta appear to be similar to the original Beta zeolite. The stability of Na-Beta framework surrounding the copper nanoparticles ensures the stable activity of the catalyst. For the control catalyst Cu/Na-Beta, however, Cu nanoparticles significantly grow up after reaction (Figure S5) and, accordingly, the catalyst, though with poor activity, deactivates in a much shorter time on stream. It should be pointed out that the copper species loaded on or enclosed in the zeolite Beta are significantly different, as shown by the measurement of H$_2$ temperature-programed

Chem
Article

CellPress

Table 2. Cu k-edge EXAFS Data for the Cu-Based Catalysts

Sample	Scattered	R(Å)[a]	CN (Cu-Cu)[b]	σ^2(Å²)[c]
Cu@Na-Beta	Cu	2.57	8.59 ± 0.86	0.0138
Cu/Na-Beta	Cu	2.54	7.74 ± 0.87	0.0136
Cu/SiO₂	Cu	2.55	10.29 ± 0.63	0.0135

All the parameters are obtained with the catalysts in reaction of CO₂+3H₂ in the XAS cell.
[a]Bond distances
[b]Coordination number
[c]Debye-Waller factor

reduction. The copper species enclosed are reduced at temperatures about 100°C higher than those loaded on the zeolite (Figure 2F). The results show that, in Cu@Na-Beta, Cu particles are tightly surrounded by a molecular sieve and interact with each other.

Operando X-ray Afine structure (XAFS) measurements were performed to determine the status of copper species during the reaction under 250°C and 0.5 MPa pressure and the results are shown in Figures 2G and 2H. The XANES spectra in Figure 2G show that as soon as reaction gas is introduced, the intensity of the peak at 8,997 eV starts to decrease, indicating the reduction of CuO. Simultaneously, the peak at 8,981.3 eV due to the Cu species appears and increases with time on stream. By the edge fitting, CuO species are reduced to Cu after 40 min on stream, indicating that metallic copper is mainly the active species for the reaction. The radial distribution functions of the copper obtained by Fourier transform of the EXAFS are shown in Figure 2H and those of the control catalysts, i.e., Cu/Na-Beta and Cu/SiO₂, are also listed. The coordination parameters of Cu in the three samples are given in Table 2. The Cu-Cu shell coordination number and distances in the three samples are given in Table 2, which shows the copper nanoparticles in Cu@Na-Beta and Cu/Na-Beta are similar in size of around ~3 nm[26,27] in accordance with the TEM results and the copper nanoparticles in Cu/SiO₂ are slightly larger in size. This means that the crystal structure of the copper nanoparticles in the three samples are in fact similar, which cannot explain their significant differences in the catalytic property for CO₂ hydrogenation. We think the true cause lay in the different shapes of the copper nanoparticles in the samples and the intimate interaction between the copper and the support. The Cu@Na-Beta has irregular copper nanoparticles and the most intimate interaction between copper and zeolite. The intimacy of copper and zeolite for Cu/Na-Beta is inferior to that of Cu@Na-Beta and only the bottoms of the copper particles contact with the zeolite and it was prepared with traditional impregnation method and without encapsulation (Figure S5). A small amount of ethanol observed on the Cu/Na-Beta may form at the boundary of copper and Na-Beta zeolite. The results of X-ray photoelectron spectroscopy (XPS) and Cu LMM Auger spectra (Figure S6) recorded with the samples reduced in the instrument show that a small amount of electropositive copper species is detected in the Cu@Na-Beta but not detected in other two samples, which implies copper particles, or the surface copper atoms in the particles, interact strongly with the framework oxygen of the Na-Beta surrounding, and, a relatively more intimate cooperation between Cu site and the zeolite of Cu@Na-Beta can be deduced.

As to the formation mechanism of CH₃CH₂OH from CO₂ hydrogenation on Cu@Na-Beta, it was explored by a transient measurement between the switching of H₂/¹²CO₂ mixture (3/1) to H₂/¹³CO₂ mixture (3/1). Under steady-state reaction conditions (300°C and 0.5 MPa), the stream of H₂/¹²CO₂ mixture (3/1) was switched to
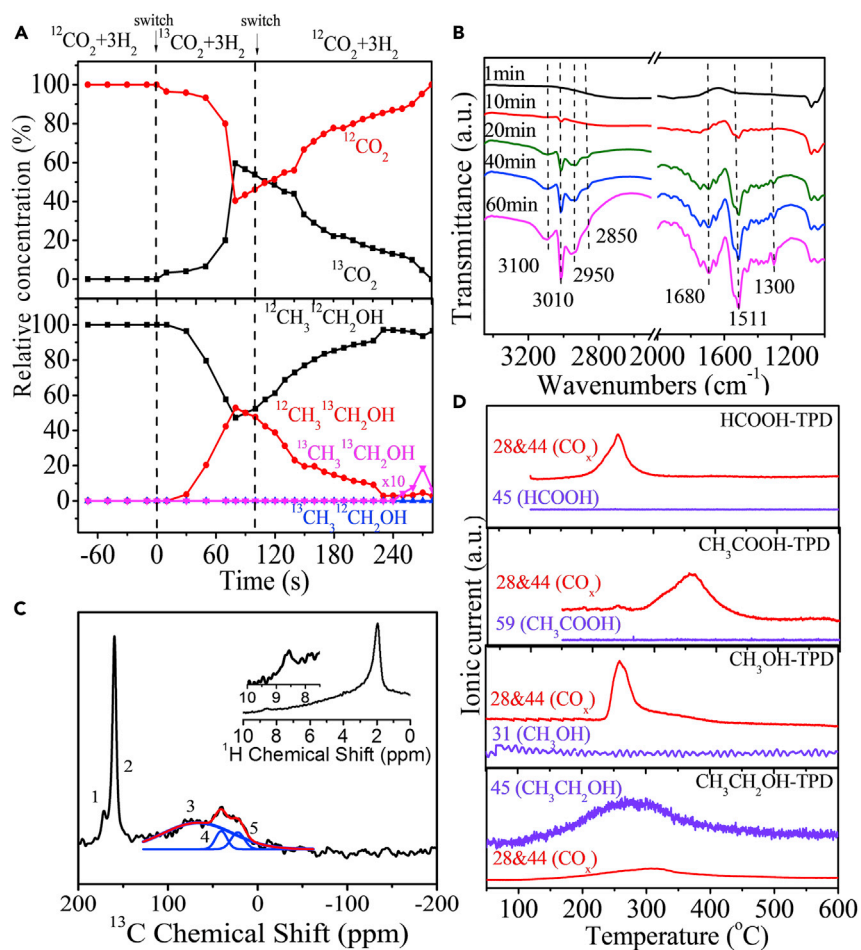
Figure 3. Investigation on the Reaction Intermediates of CO₂ to CH₃CH₂OH on Cu@Na-Beta Catalyst

(A) The relative concentrations, monitored at the outlet of the reactor, of $^{13}CO_2$ or $^{12}CO_2$ during switching the reactants between $^{13}CO_2+3H_2$ and $^{12}CO_2+3H_2$ (up panel); and concentrations of products ($^{12}CH_3{}^{12}CH_2OH$, black; $^{12}CH_3{}^{13}CH_2OH$, red; $^{13}CH_3{}^{12}CH_2OH$, blue; and $^{13}CH_3{}^{13}CH_2OH$, pink) during the switching (lower panel), over the catalyst Cu@Na-Beta in reaction.

(B) *In situ* FT-IR spectrum during exposure of Cu@Na-Beta to 0.7 MPa reaction gas (CO_2/H_2 = 1:3) at 300°C. CH_3COO^-:3,010 cm^{-1} δ(CH), 1,680 cm^{-1} ν$_{as}$(OCO), 1,511 cm^{-1} ν$_s$(OCO); CH_3CH_2OH: ν$_s$(OH) 3,100 cm^{-1}, 1,300 cm^{-1}δ(OH), 2,850 cm^{-1} ν$_s$(CH$_2$), and 2,950 cm^{-1} ν$_{as}$(CH$_2$).

(C) The ^{1}H→^{13}C CP MAS NMR and 1H MAS NMR recorded on the catalyst quenched from steady-state reaction on stream of $H_2/^{13}CO_2$ (3/1).

(D) TPD profiles detected using a mass spectrometer from the catalyst Cu@Na-Beta with adsorption of HCOOH, CH₃COOH, CH₃OH, and CH₃CH₂OH, respectively.

$H_2/^{13}CO_2$ mixture (3/1) and then switched back to the original $H_2/^{12}CO_2$ mixture (3/1) gases. The products at the exit of the reactor were stored using a multiposition micro-electric valve actuators with 12 sample loops of 500 μl and analyzed afterward by a GC-MS (Figure S7), and the results are shown in Figure 3. The products of $^{12}CH_3{}^{12}CH_2OH$, $^{12}CH_3{}^{13}CH_2OH$, $^{13}CH_3{}^{12}CH_2OH$, and $^{13}CH_3{}^{13}CH_2OH$ are detected by their characteristic m/z peaks listed in Table S1. The changes in the relative concentration of $^{13}CO_2$ and $^{12}CO_2$ respond to the transient switching accordingly. The most important result is the synchronous variation of $^{12}CH_3{}^{13}CH_2OH$ signal with the $^{13}CO_2$ along the switching time (Figure 3), suggesting that the gaseous $^{13}CO_2$ reacts with surface $^{12}CH_3*$ readily to give $^{12}CH_3{}^{13}CH_2OH$. The results also imply that the

Chem
Article

CellPress

formation of C–C bond over this catalyst is in fact faster than the formation of C1 species, such as methane, coincident with the results of the catalytic reaction listed in Figure 1. The surface $^{12}CH_3$* species can be inferred on the copper catalyst surface because methane is a common product of CO_2 hydrogenation on copper-based catalysts.[23]
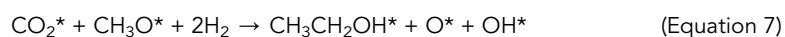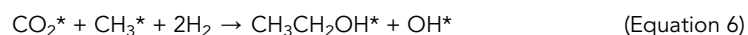
For further detection of the surface intermediates, the measurements of *in situ* FT-IR on Cu@Na-Beta were applied. The wavenumbers of 3,010 cm^{-1} δ(CH), 1,680 cm^{-1} ν_{as}(OCO), and 1,511 cm^{-1} ν_s(OCO) can be assigned to adsorbed CH_3COO* and the wavenumbers of 3,100 cm^{-1} ν_s(OH), 1,300 cm^{-1} δ(OH), 2,850 cm^{-1} $\nu_s(CH_2)$, and 2,950 cm^{-1} $\nu_{as}(CH_2)$ can be assigned to CH_3CH_2OH [9a] (Figure 3B). For comparison, the results of similar measurements on Cu/Na-Beta are shown in Figure S8. In general, the differences are obvious, such as the much weaker signals of CH_3COO* and different distribution of surface species, in accordance with its lower activity for CO_2 hydrogenation to produce a small amount of CH_3OH, CH_4, and CH_3CH_2OH.

The catalyst was rapidly quenched to room temperature from steady-state reaction at 250°C and the surface species were then detected by NMR for ^{13}C-NMR measurement, the Cu@Na-Beta was quenched from steady-state reaction and then loaded in a glove box to an solid state NMR rotor. The results of NMR measurement are depicted in Figure 3C. The ^{13}C NMR signal at 160.0 ppm (peak 2) and the ^{1}H NMR peak at 8.6 ppm (trace hydrogen attached to a carboxyl group) are consistent with the presence of carboxyl species. The ^{13}C NMR resonance at 60.7 ppm (peak 3) suggests the presence of surface methoxy species while the other signals observed at 20.9 (peak 4),39.7 ppm (peak 5), and 1~3 ppm (^{1}H NMR) are in agreement with the formation of different surface methyl species.[4] The ^{13}C NMR signal at 170.0 ppm (peak 1) is assigned to carbonate, which is not so important in the reaction. It is suggested by the results of IR and NMR that the intermediate for ethanol is surface-adsorbed acetic acid, i.e., *CH_3 + O=C=O* à CH_3COO* + *. The energy barrier for desorption of the intermediate acetate radical is too high,[28] which can only be hydrogenated to ethanol in further steps.

As to the reason for that the methanol, formic acid, or acetic acid is not detected in the product during the steady-state reaction of CO_2 hydrogenation, the constraint of the zeolite Na-Beta framework surrounding the copper nanoclusters must take effect. As shown in Figure 3D, basically no CH_3OH, $HCOOH$, or CH_3COOH can be detected by a mass spectrometer, during heating the catalyst, Cu@Na-Beta, with the adsorption of CH_3OH, $HCOOH$, or CH_3COOH, respectively, which all decomposed to CO_x during the heating of temperature-programmed desorption (TPD), indicative of the strong interaction of the compounds with the catalyst. The ethanol, however, can desorb successfully from the catalyst around 200°C ~300°C. Interestingly, no CH_3OH, $HCOOH$, or CH_3COOH can be detected by the mass spectrometer, during heating the catalyst Cu/Na-Beta with the adsorption of CH_3OH, $HCOOH$, or CH_3COOH, respectively, which all decomposed to CO_x during the heating of TPD. Even most of ethanol decomposed to CO_x (Figure S8B). The results indicate the strong adsorption of the zeolite to these species.

To shed insightful light on the mechanism of ethanol formation, density functional and slab model calculations were performed on the two key and crucial steps for this process: the formation of surface methyl and the C–C bond. Many documented results on copper-based catalysts catalyzed CO_2 hydrogenation indicate that methyl is likely formed from CH_3OH and/or CH_3O whose formation is quite facile

 CellPress

as demonstrated by Kattel et al.[18] Hence, we considered the pathways (Equation 4) and (Equation 5) for CH$_3$ formation on the model surfaces. Reactions (Equation 6) and (Equation 7) were designed for C–C bond formation.

$$CH_3O^* \rightarrow CH_3^* + O^* \qquad \text{(Equation 4)}$$

$$CH_3OH^* \rightarrow CH_3^* + OH^* \qquad \text{(Equation 5)}$$

$$CO_2^* + CH_3^* + 2H_2 \rightarrow CH_3CH_2OH^* + OH^* \qquad \text{(Equation 6)}$$

$$CO_2^* + CH_3O^* + 2H_2 \rightarrow CH_3CH_2OH^* + O^* + OH^* \qquad \text{(Equation 7)}$$

Test calculations show that the (100), (110), and (111) facets of copper were not active enough for the reactions. The (221) facet of copper, which was observed on the copper nanoparticles (Figure 2), was found to be effective and, thus, was selected to mimic the catalyst. To better reflect the real catalyst surface, three (221) surface models were constructed, i.e., the perfect, with Cu vacancy or O-doped at the edge (Figure 4A,). The obtained binding energies for CO$_2$ on the three surfaces are 0.31, 0.39, and 0.47 eV, respectively.

Figures 4B–4D illustrate the initial states (IS), transition states (TS), and final states (FS) of the kinetically favorable pathways for reactions (Equation 4) and (Equation 5). Other pathways are depicted in Figure S9. Surface defects, vacancy, and doped atoms, reduce the barriers by 0.2–0.3 eV, as shown in Table S2. The barrier/reaction heat calculated for a kinetically favorable route of CH$_3$O* → CH$_3$* + O* is 0.99/0.57 eV for the O-doped Cu (221). Methyl formation via the C–O bond breaking of CH$_3$OH is easier than through CH$_3$O decomposition. The two lowest barriers are 0.78 eV with exothermicity of −0.35 on the O-doped surface (Table S2). A similar route that has 0.80 eV for the barrier and −0.36 for the reaction heat is calculated on the Cu vacant Cu (221). These results indicate that the formed methanol can be easily converted into methyl, consistent with undetectable methanol in the product. When zero-point energy (ZPE) correction is included, the barriers are only 0.68 eV. A similar route that has 0.80 (0.70 with ZPE correction) eV for the barrier and −0.36 for the reaction heat is calculated on the Cu vacant Cu(221). These results indicate that the formed methanol can be easily converted into methyl, consistent with undetectable methanol in the product.

For the reactions (Equation 6) and (Equation 7), the initial states, transition states, and final states of CO$_2$* + CH$_3$* + 2H$_2$ reaction paths on the three (221) surfaces are depicted in Figures 4E–4G, respectively. The reaction CO$_2$ + CH$_3$O + 2H$_2$ on the three (221) surfaces are depicted in Figure S9 of Supplemental Information. Figures 4H and 4I show the calculated energy barriers/reaction energies without zero-point energy correction for CO$_2$* + CH$_3$* → CH$_3$COO* on the perfect, Cu vacancy, and O-doped defect surfaces are ④ 0.32/−1.43, ⑤ 0.19/−1.49, and ⑥ 1.49/−0.05 eV, respectively. The reaction energies ⑦ for CH$_3$COO* reduction to CH$_3$CH$_2$OH* are −1.17,−0.67, and −0.92 eV on the corresponding (221) surfaces, respectively. The reactions are exothermic. Figure 4J shows the energy barriers/reaction energies for the reaction CO$_2$* + CH$_3$O* + 2H$_2$ on the three model (221) surfaces.

Chem
Article

CellPress
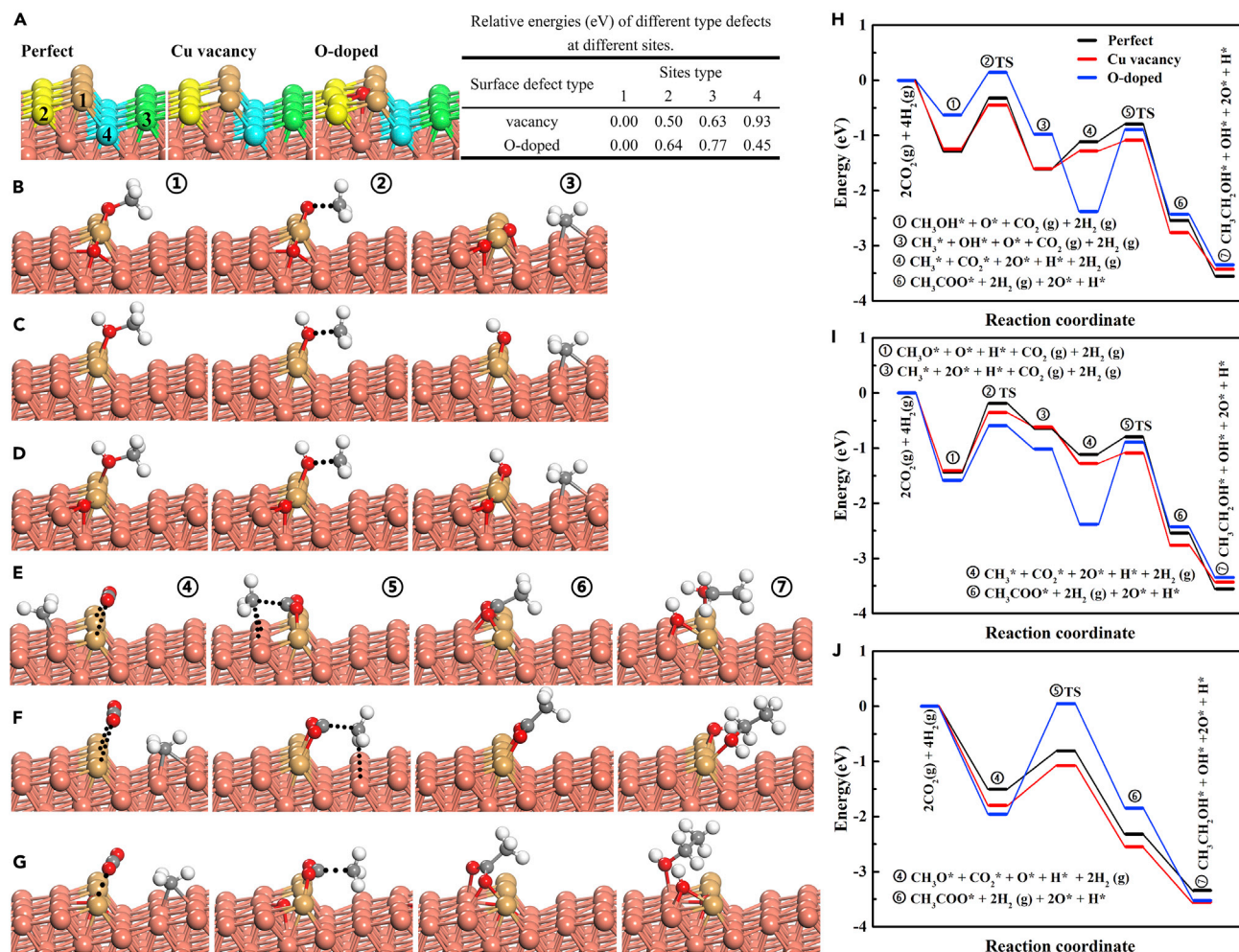

Figure 4. Reaction Pathway of CO₂ to CH₃CH₂OH and Reaction Energetics Calculated by DFT

(A) Illustrations of perfect, Cu vacancy, and O-doped surfaces on the edges. The differently colored atoms represent different sites on first layer (yellowish-brown for site type 1, yellow for site type 2, green for site type 3, and blue for site type 4. Dark brown sphere is for Cu at lower layers).

(B–D) Illustrations of the initial state, transition state, and final state of methyl formation from CH₃O* on (B) O-doped Cu(221) and from CH₃OH on (C) Cu vacancy defect surface and (D) O-doped surface.

(E–J) Illustrations of the initial state, transition state, and final state of CO₂+CH₃ reaction paths on (E) Cu vacancy defect surface, (F) perfect surface, (G) O-doped surface and potential energy surfaces for the reaction of (H) CO₂ + CH₃OH → CO₂ + CH₃ → CH₃CH₂OH, (I) CO₂ + CH₃O → CO₂ + CH₃ → CH₃CH₂OH, and (J) CO₂ + CH₃O → CH₃CH₂OH. Dark brown sphere, Cu; red sphere, O; gray sphere, C; white sphere, H; yellowish-brown, Cu on edge.

As can be seen from the results, all the steps are exothermic except the reaction CO₂*+CH₃O* to CH₃COO* on the O-doped defect (221) surface, which is slightly endothermic. For CO₂* + CH₃* to CH₃COO*, the Cu vacancy surface is very favorable for this process with a barrier of 0.19 eV that is smaller than the adsorption energy of CO₂ (0.39 eV), followed by the perfect surface with the barrier of 0.32 eV and CO₂ adsorption energy of 0.31 eV. The high barrier of 1.49 eV on the O-doped surface indicates that the reaction hardly takes place here. For CO₂* + CH₃O* to CH₃COO*, the barrier heights on the three models are larger than the calculated adsorption energy of CO₂. Hence, CO₂ would desorb before reacting with CH₃O*. These results suggest that the C–C bond forms mainly from the reaction of CO₂ with methyl (not methoxide) and the step surface with Cu vacancy is the most effective sites for the rapid bonding of CO₂* to surface methyl species to

CellPress
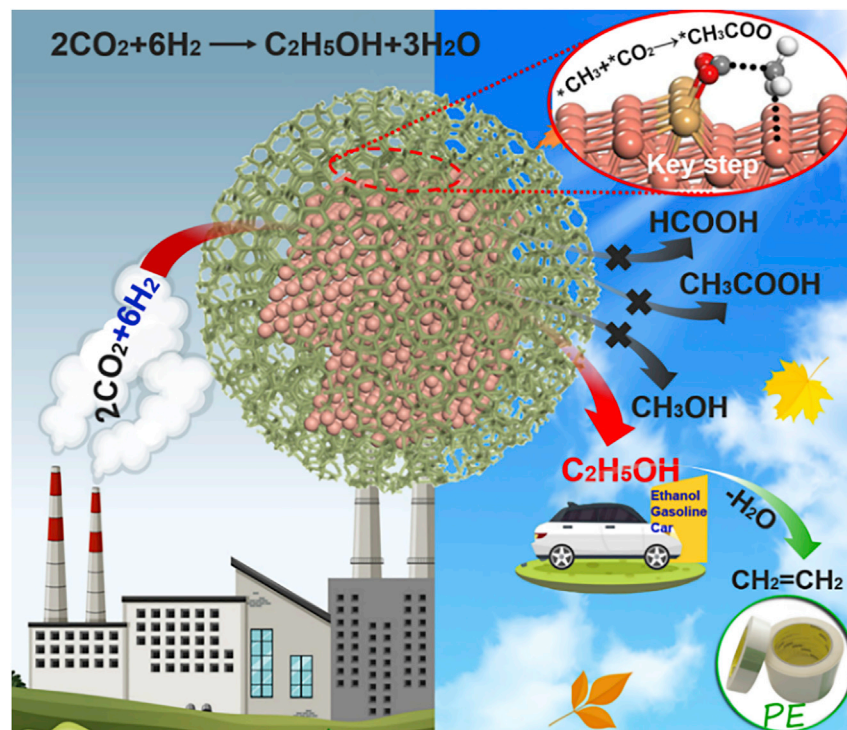
Chem
Article

Scheme 1. Summary of the CO$_2$ Hydrogenation to Ethanol over the Catalyst Cu@Na-Beta

The active copper nanoparticles were enclosed in the zeolite particles in irregular shapes constrained by the zeolite mesopores purposely prepared by alkali etching. At such nanoparticles of copper, step surfaces can be stabilized by the intimate constraint of the zeolite, which are active for the bonding of CO$_2$ with adsorbed methyl to form intermediate CH$_3$COO*, which is converted to ethanol in following hydrogenation.

form surface acetyl acid which converts to the final product of ethanol in following exothermic hydrogenations.

Now, in phenomenology, the hydrogenation of CO$_2$ to CH$_3$CH$_2$OH occurs at the reactive centers of copper nanoparticles in irregular shapes, which are shaped and confined by the 3D Na-Beta zeolitic frameworks from all sides. The reaction process can be summarized and shown in Scheme 1. The unique copper nanoparticles in irregular shapes with step surface and the intimate cooperation between Cu nanoparticles and Na-Beta play the key role in the high performance of reaction over the catalyst Cu@Na-Beta. CO$_2$ is firstly hydrogenated to CH$_3$* at the surface of copper nanoparticles and the subsequent CO$_2$* adsorbed reacts with CH$_3$* to form CH$_3$COO* as the most important surface intermediate, which cannot desorb directly due to the high thermodynamics barrier.[29] The followed hydrogenation of CH$_3$COO* to ethanol is exotic and easy to take place on the catalyst.[30] The 3D Na-Beta zeolitic framework functions at two aspects, i.e., to confine and modulate the copper nanoparticals in unique shapes with surface sites for the reactions and to constrain the reactants at the layer nearby the nanoparticle surface to restrict the formation of by-products such as methanol, formic acid, or acetic acid.

Conclusion

In conclusion, CO$_2$ can be converted to ethanol in high efficiency over the complex catalyst Cu@Na-Beta. Combining the experimental and theoretical calculation

Chem
Article

CellPress

results, it is considered that the synergies between the irregular copper nanoparticles and the surrounding zeolitic framework are responsible for the high-performance catalyst Cu@Na-Beta. The current findings reflect the importance of the catalytic assembly of "reactive centers plus their surroundings" that would be extracted as a new concept of mesocatalyst, and the appropriate use of such combinatory structures will be great helpful to design more highly efficient catalysts.

EXPERIMENTAL PROCEDURES

Resource Availability

Lead Contact

Weiping Ding is the Lead Contact for this work and can be reached here: dingwp@nju.edu.cn.

Materials Availability

All materials generated in this study are being made available.

Data and Code Availability

The published article includes all Data and Code generated or analyzed during this study.

Preparation of Catalysts

In a typical synthesis of Cu@Na-Beta, 6.00 g commercial Na-Beta zeolites (Si/Al ~ 25) in a size of ~0.1 μm were introduced intracrystalline mesopores by alkaline treatment with 200ml 0.200mol/L NaOH solution at 65°C for 30 min, then filtered, washed, and dried (denoted as alk-Beta). Then CuO was introduced in the pores of alk-Beta by impregnating Cu(NO$_3$)$_2$ ethanol solution and then calcined at 450°C for 3 h (denoted as CuO/alk-Beta). Then in the next step, 1.00 g CuO/alk-Beta was thoroughly mixed with a kind of Na-Beta zeolite synthesis gel, which was prepared by 0.125 g Al$_2$(SO$_4$)$_3$·18H$_2$O, 3.16 g 20% Tetraethylammonium hydroxide (TEAOH), 0.540g SiO$_2$, and 0.0275g NaOH. The slurry was treated at 180°C for 2 days for crystallization using the dry gel conversion method as we previously reported[19] and then thoroughly rinsed with water and calcined at 550°C for 4 h in air to remove the template, and the sample was denoted as CuO@Na-Beta. The CuO@Na-Beta was reduced by 5% H$_2$/N$_2$ at 350°C for 1.5 h before the catalytic test (denoted as Cu@Na-Beta). CuO@Na-ZSM-5 and Cu@Na-ZSM-5 were prepared similarly with Na-ZSM-5. The CuO/Na-Beta and CuO/SiO$_2$ were prepared by traditional impregnation method. Cu(NO$_3$)$_2$ ethanol solution was impregnated to Na-Beta zeolite or SiO$_2$ (Cu: Na-Beta or SiO$_2$ = 82.4 mg: 917.6 mg) and then calcined at 450°C for 3 h to be CuO/Na-Beta or CuO/SiO$_2$, which were reduced to Cu/Na-Beta or Cu/SiO$_2$ by 5% H$_2$/N$_2$ at 350°C for 1.5 h before the catalytic test. The copper contents in all the samples were controlled as the same for the convenience of comparison.

Characterization of Catalysts

The crystalline structure and morphology of the catalysts were characterization by XRD, TEM, and HRTEM. XRD measurements were performed on an X'pert PAN analytical diffractometer (Cu Kα radiation, 40 kV, 40 mA). TEM and HAADF-STEM images of the samples were obtained using JEM-2010 UHR and FEI Tecnai G2F20 (200 kV). The status of Cu in the samples during the reduction and reaction in the mixed gases of CO$_2$ + 3H$_2$ at 250°C and 0.5 MPa was determined by *in situ* measurement of Cu K-edge X-ray absorption spectra (XANES and EXAFS). These data were acquired in transmission mode at beamline BL14W1 (Shanghai Synchrotron Radiation Facility). The station was operated with a Si (111) double crystal

monochromator. Around 100 mg sample was pressed into 1cm wafer and placed in an *in situ* cell attached to a controlled heating equipment. Gas flows were controlled by mass flow controllers. The valence states of Cu in Cu@Na-Beta were also carefully analyzed by XPS and AES (Auger electron spectroscopy). For the measurement, the catalyst was treated at 250°C in flowing CO_2 + 3H_2 at 0.5 MPa for 40 min and then transferred into XPS chamber without contacting air.

The H_2 temperature-programmed reduction was carried out at apparatus TP5080 (Xianquan, Tianjin). The sample, placed in a quartz tube, was pretreated at 200°C in Ar for 1 h and cooled down to room temperature. Then the sample was heated in flowing 5% H_2/Ar at 10°C/min, and the consumption of H_2 was monitored using a thermal conductivity detector. CH_3OH, CH_3CH_2OH, HCOOH, or CH_3COOH temperature-programmed desorption were measured using the same apparatus. The catalyst was firstly pretreated and reduced at 350°C. After cooled down to room temperature, the compounds of CH_3OH, CH_3CH_2OH, HCOOH, and CH_3COOH were introduced into the carrier gas at 70°C to the catalyst for adsorption, respectively. Then, the desorbed species from the catalyst were monitored by a mass spectrometer during linear heating in flowing He at 10°C/min.

Switching Experiment between H_2/$^{12}CO_2$ Mixture (3:1) and H_2/$^{13}CO_2$ Mixture (3:1)

Figure S6 shows the schematic drawing of equipment with a computer-controlled twelve-position valve with sample loops specifically designed for collecting multiple compositions at short time intervals of the product gas at transient state for later GC-MS analysis. Under steady-state conditions (250°C and 0.5 MPa), the stream of H_2/$^{12}CO_2$ mixture (3:1) was switched to H_2/$^{13}CO_2$ mixture (3:1) and then switched back to the original H_2/$^{12}CO_2$ mixture (3:1) gases. The products at various time of transient at the exit of the reactor were stored in the 12 sample loops of 500 μl and analyzed afterward by GC-MS.

NMR and IR Detection on Quenched Catalyst

The Cu@Na-Beta during the steady-state reaction with H_2/$^{13}CO_2$ mixture (3:1) at 250°C for 0.5 h, 0.5 MPa was quenched rapidly to room temperature and loaded in a glove box to a solid-state NMR rotor for ^{1}H MAS NMR or ^{1}Hà^{13}C CP MASNMR measurements. For IR detection, the Cu@Na-Beta was similarly quenched from steady-state reaction to room temperature with H_2/$^{12}CO_2$ (3:1) as reaction gas. Then the sample was placed in a quartz cell for IR measurement.

Catalytic Tests

CO₂ hydrogenation was carried out in a fixed-bed reactor with 6 mm inner diameter. 0.10 g catalyst (pelletized and sieved into 0.38–0.83 mm particles) was packed in the reactor and rested in the middle of the furnace heating zone. After reduction of the catalyst at 350°C in the reactor by 5% H_2/N_2 gas flow (20 ml/min) for 1.5 h, the reactor was charged with a H_2/CO_2 mixed gas (3:1, and 8% N_2 as internal standard) at various flows and pressures. The products were analyzed by online GC with dual column and dual detector. CO_2, H_2, N_2, CO, and light alkane were separated by TDX-01 and detected by Thermal conductivity detector (TCD), while alcohols or hydrocarbons were separated by supelco Petrocol DH 50.2 chromatographic column and detected by FID.

CO_2 conversion was calculated by equation:

CO_2 conversion = CO_2 conversion was calculated by equation:

$$CO_2 \text{ conversion} = \frac{CO_{2in} - CO_{2out}}{CO_{2in}} \times 100\%$$

where CO$_{2\ in}$ and CO$_{2\ out}$ represent the molar fraction of CO$_2$ at the inlet and outlet, respectively.

Product selectivities were calculated according to equations:

$$S(CO) = \frac{CO_{2out}}{CO_{2in} - CO_{2out}} \times 100\%$$

$$S(CH_3OH) = \frac{f_{CH_3OH}A_{CH_3OH}}{f_{CH_3OH}A_{CH_3OH} + f_{CH_4}A_{CH_4} + 2f_{CH_3CH_2OH}A_{CH_3CH_2OH}} \times 100\%$$

$$S(CH_4) = \frac{f_{CH_4}A_{CH_4}}{f_{CH_3OH}A_{CH_3OH} + f_{CH_4}A_{CH_4} + 2f_{CH_3CH_2OH}A_{CH_3CH_2OH}} \times 100\%$$

$$S(CH_3CH_2OH) = \frac{2f_{CH_3CH_2OH}A_{CH_3CH_2OH}}{f_{CH_3OH}A_{CH_3OH} + f_{CH_4}A_{CH_4} + 2f_{CH_3CH_2OH}A_{CH_3CH_2OH}} \times 100\%$$

S(CH$_3$OH), S(CH$_3$CH$_2$OH), S(CH$_4$) were calculated in organic products exclude CO.

where CO$_{2\ in}$ and CO$_{2\ out}$ represent the molar fraction of CO$_2$ at the inlet and outlet, respectively.

Theoretical Calculations

All the calculations were performed using the Vienna *ab initio* simulation package (VASP)[31] in the generalized gradient approximation (GGA-PBE). A plane-wave basis set with a cutoff energy of 450 eV and a (3 × 5 × 1) k-point grid generated with the Monkhorst-Pack scheme[32] were used. The atomic positions were relaxed until the forces on all unconstrained atoms were ≤0.02 eV/Å. DFT-D3 scheme[33] for corrections of dispersion interactions and the DFT+U that better describes the localized d electrons with U = 5.0 eV for Cu were employed. The copper catalyst was modeled with Cu (221) surface which in the perfect surface model contains 64 Cu atoms built from the theoretically optimized cubic bulk Cu structure with a lattice parameter a = 3.61 Å using (15 × 15 × 15) k-point grid. This optimized bulk parameter agrees with the experimental value of 3.61 Å very well.[34] Two defect surface models were constructed (Figure 4). A vacuum space of at least 10 Å thickness was applied to avoid artificial interactions between the slab and its periodic neighbors. In all calculations, the bottom two stepped layers having 32 Cu atoms were fixed at their equilibrium bulk positions, whereas the atoms in the top two layers together with the adsorbates were allowed to fully relax. Transition states were located using the nudged elastic band (NEB) method[35] and verified by the presence of one and only one imaginary frequency corresponding to the C–C bond formation/breaking while there were no imaginary frequencies at all for the initial and final states.

The relative stabilities of defect surfaces were first studied. Two defect types, Cu vacancy and O-doped, were considered. Figure 4 depicts the perfect surface (B), defect surfaces with Cu vacancy (C), and O-doped (D) defects. The first layer Cu atoms were colored differently to represent four unequal surface sites. The positions of defects (vacancy and doped site) were determined by comparing the stability of the defect locating at row 1 to row 4 (see Figure 4). Both Cu vacancy and doped oxygen atom prefer the edge sites (Figure 4).

All bond lengths and O–C–O angles of CO_2* in Figures 4 and S9 were listed in Table S3.

SUPPLEMENTAL INFORMATION

Supplemental Information can be found online at https://doi.org/10.1016/j.chempr.2020.07.001.

AUTHOR CONTRIBUTIONS

W.D. conceived and organized the work. L.D., J.G., Y.C., and Z.Z. designed and joined the experiments. L.D. performed the main experiments. Z.C. and T.S. performed the theoretical calculations. M.L. and P.W. participated in the TEM experiments. C.Y. and L.P. carried out the NMR analysis. T.C. and Y.Z. helped the EXAFS measurements and data processing. N.X. and X.G. joined discussions. L.D. and W.D. wrote the manuscript, and W.D. finalized the work. All authors discussed the results.

DECLARATION OF INTERESTS

The authors declare no competing interests.

REFERENCES

1. Enthaler, S., von Langermann, J., and Schmidt, T. (2010). Carbon dioxide and formic acid—the couple for environmental-friendly hydrogen storage? Energy Environ. Sci. 3, 1207–1217.

2. Ghoniem, A.F. (2011). Needs, resources and climate change: clean and efficient conversion technologies. Prog. Energy Combust. Sci. 37, 15–51.

3. Moret, S., Dyson, P.J., and Laurenczy, G. (2014). Direct synthesis of formic acid from carbon dioxide by hydrogenation in acidic media. Nat. Commun. 5, 4017.

4. Larmier, K., Liao, W.C., Tada, S., Lam, E., Verel, R., Bansode, A., Urakawa, A., Comas-Vives, A., and Copéret, C. (2017). CO₂-to-methanol hydrogenation on zirconia-supported copper nanoparticles: reaction intermediates and the role of the metal-support interface. Angew. Chem. Int. Ed. 56, 2318–2323.

5. An, B., Zhang, J., Cheng, K., Ji, P., Wang, C., and Lin, W. (2017). Confinement of ultrasmall Cu/ZnOx nanoparticles in metal–organic frameworks for selective methanol synthesis from catalytic hydrogenation of CO₂. J. Am. Chem. Soc. 139, 3834–3840.

6. Spivey, J.J., and Egbebi, A. (2007). Heterogeneous catalytic synthesis of ethanol from biomass-derived syngas. Chem. Soc. Rev. 36, 1514–1528.

7. Kusama, H., Okabe, K., Sayama, K., and Arakawa, H. (1997). Ethanol synthesis by catalytic hydrogenation of CO₂ over Rh-FeSiO2 catalysts. Energy 22, 343–348.

8. Nieskens, D.L.S., Ferrari, D., Liu, Y., and Kolonko, R. (2011). The conversion of carbon dioxide and hydrogen into methanol and higher alcohols. Catal. Commun. 14, 111–113.

9. Li, S., Guo, H., Luo, C., Zhang, H., Xiong, L., Chen, X., and Ma, L. (2013). Effect of iron promoter on structure and performance of K/Cu–Zn catalyst for higher alcohols synthesis from CO₂ hydrogenation. Catal. Lett. 143, 345–355.

10. Prieto, G., Beijer, S., Smith, M.L., He, M., Au, Y., Wang, Z., Bruce, D.A., de Jong, K.P., Spivey, J.J., and de Jongh, P.E. (2014). Design and synthesis of copper-cobalt catalysts for the selective conversion of synthesis gas to ethanol and higher alcohols. Angew. Chem. Int. Ed. 53, 6397–6401.

11. He, Z., Qian, Q., Ma, J., Meng, Q., Zhou, H., Song, J., Liu, Z., and Han, B. (2016). Water-enhanced synthesis of higher alcohols from CO₂ hydrogenation over a Pt/Co₃O₄ catalyst under milder conditions. Angew. Chem. Int. Ed. 55, 737–741.

12. Chen, Y., Choi, S., and Thompson, L.T. (2016). Low temperature CO₂ hydrogenation to alcohols and hydrocarbons over Mo₂C

Chem
Article

🔾 **CellPress**

supported metal catalysts. J. Catal. 343, 147–156.

13. Bai, S., Shao, Q., Wang, P., Dai, Q., Wang, X., and Huang, X. (2017). Highly active and selective hydrogenation of CO_2 to ethanol by ordered Pd–Cu nanoparticles. J. Am. Chem. Soc. 139, 6827–6830.

14. Wang, L., Wang, L., Zhang, J., Liu, X., Wang, H., Zhang, W., Yang, Q., Ma, J., Dong, X., Yoo, S.J., et al. (2018). Selective hydrogenation of CO_2 to ethanol over cobalt catalysts. Angew. Chem. Int. Ed. 57, 6104–6108.

15. Song, Y., Chen, W., Zhao, C., Li, S., Wei, W., and Sun, Y. (2017). Metal-free nitrogen-doped mesoporous carbon for electroreduction of CO_2 to ethanol. Angew. Chem. Int. Ed. 56, 10840–10844.

16. Liao, F., Huang, Y., Ge, J., Zheng, W., Tedsree, K., Collier, P., Hong, X., and Tsang, S.C. (2011). Morphology-dependent interactions of ZnO with Cu nanoparticles at the materials' interface in selective hydrogenation of CO_2 to CH_3OH. Angew. Chem. Int. Ed. 50, 2162–2165.

17. Su, J., Zhang, Z., Fu, D., Liu, D., Xu, X.-C., Shi, B., Wang, X., Si, R., Jiang, Z., Xu, J., and Han, Y.-F. (2016). Higher alcohols synthesis from syngas over CoCu/SiO_2 catalysts: dynamic structure and the role of Cu. J. Catal. 336, 94–106.

18. Kattel, S., Ramírez, P.J., Chen, J.G., Rodriguez, J.A., and Liu, P. (2017). Active sites for CO_2 hydrogenation to methanol on Cu/ZnO catalysts. Science 355, 1296–1299.

19. Gu, J., Zhang, Z., Hu, P., Ding, L., Xue, N., Peng, L., Guo, X., Lin, M., and Ding, W. (2015). Platinum nanoparticles encapsulated in MFI zeolite crystals by a two-step dry gel conversion method as a highly selective hydrogenation catalyst. ACS Catal. 5, 6893–6901.

20. Li, L., Lv, J., Shen, Y., Guo, X., Peng, L., Xie, Z., and Ding, W. (2014). Hexadecylphosphate-Functionalized iron oxide nanoparticles: mild oxidation of benzyl C–H bonds exclusive to carbonyls by molecular oxygen. ACS Catal. 4, 2746–2752.

21. Liu, L., Díaz, U., Arenal, R., Agostini, G., Concepción, P., and Corma, A. (2017). Generation of subnanometric platinum with high stability during transformation of a 2D zeolite into 3D. Nat. Mater. 16, 132–138.

22. Zhang, Z., Li, Y., Gu, J., Ding, L., Xue, N., Peng, L., Guo, X., Zhu, Y., Ma, J., and Ding, W. (2018). The effect of electrostatic field on the catalytic properties of platinum clusters confined in zeolite for hydrogenation. Catal. Sci. Technol. 8, 6384–6395.

23. Wang, Z., Xu, Z.N., Peng, S.Y., Zhang, M.J., Lu, G., Chen, Q.S., Chen, Y., and Guo, G.C. (2015). High-performance and long-lived Cu/SiO_2 nanocatalyst for CO_2 hydrogenation. ACS Catal. 5, 4255–4259.

24. Jiao, F., Li, J., Pan, X., Xiao, J., Li, H., Ma, H., Wei, M., Pan, Y., Zhou, Z., Li, M., et al. (2016). Selective conversion of syngas to light olefins. Science 351, 1065–1068.

25. Cheng, K., Gu, B., Liu, X., Kang, J., Zhang, Q., and Wang, Y. (2016). Direct and highly selective conversion of synthesis gas into lower olefins: design of a bifunctional catalyst combining methanol synthesis and carbon–carbon coupling. Angew. Chem. Int. Ed. 55, 4725–4728.

26. Bersani, M., Gupta, K., Mishra, A.K., Lanza, R., Taylor, S.F.R., Islam, H.-U., Hollingsworth, N., Hardacre, C., de Leeuw, N.H., and Darr, J.A. (2016). Combined EXAFS, XRD, DRIFTS, and DFT study of Nano copper-based catalysts for CO_2 hydrogenation. ACS Catal. 6, 5823–5833.

27. Márquez, F., and Palomares, A. (2001). EXFAS electron spectroscopy as a new tool of local characterisation of copper in Cu-Beta zeolite. Solid State Sci. 3, 637–640.

28. Graciani, J., Mudiyanselage, K., Xu, F., Baber, A.E., Evans, J., Senanayake, S.D., Stacchiola, D.J., Liu, P., Hrbek, J., Fernández Sanz, J., and Rodriguez, J.A. (2014). Catalysis. Highly active copper-ceria and copper-ceria-titania catalysts for methanol synthesis from CO_2. Science 345, 546–550.

29. Zhao, Y.T., Cui, C.N., Han, J.Y., Wang, H., Zhu, X.L., and Ge, Q.F. (2016). Direct C–C coupling of CO_2 and the Methyl Group from CH_4 activation through facile insertion of CO_2 into Zn–CH_3σ-bond. J. Am. Chem. Soc. 138, 10191–10198.

30. Zhang, M., Yao, R., Jiang, H., Li, G., and Chen, Y. (2017). Insights into the mechanism of acetic acid hydrogenation to ethanol on Cu (111) surface. Appl. Surf. Sci. 412, 342–349.

31. Kresse, G., and Hafner, J. (1993). Ab initiomolecular dynamics for liquid metals. Phys. Rev. B 47, 558–561.

32. Monkhorst, H.J., and Pack, J.D. (1976). Special points for Brillouin-zone integrations. Phys. Rev. B 13, 5188–5192.

33. Grimme, S., Antony, J., Ehrlich, S., and Krieg, H. (2010). A consistent and accurate ab initio parametrization of density functional dispersion correction (DFT-D) for the 94 elements H-Pu. J. Chem. Phys. 132, 154104.

34. Straumanis, M.E., and Yu, L.S. (1969). Lattice parameters, densities, expansion coefficients and perfection of structure of Cu and of Cu-in α phase. Acta Crystallogr. A 25, 676–682.

35. Henkelman, G., and Jónsson, H. (2000). Improved tangent estimate in the nudged elastic band method for finding minimum energy paths and saddle points. J. Chem. Phys. 113, 9978–9985.